J. Fluid Mech. (1999), *vol.* 399, *pp.* 277–300. Printed in the United Kingdom

Bow and stern flows with constant vorticity

By SCOTT W. McCUE† AND LAWRENCE K. FORBES
Department of Mathematics, University of Queensland, Queensland 4072, Australia

(Received 30 September 1997 and in revised form 5 July 1999)

Free surface flows of a rotational fluid past a two-dimensional semi-infinite body are considered. The fluid is assumed to be inviscid, incompressible, and of finite depth. A boundary integral method is used to solve the problem for the case where the free surface meets the body at a stagnation point. Supercritical solutions which satisfy the radiation condition are found for various values of the Froude number and the dimensionless vorticity. Subcritical solutions are also found; however these solutions violate the radiation condition and are characterized by a train of waves upstream. It is shown numerically that the amplitude of these waves increases as each of the Froude number, vorticity and height of the body above the bottom increases.

1. Introduction

This paper is concerned with the two-dimensional flow of an inviscid, incompressible fluid past the bow or stern of a ship. We consider the case when the fluid is of finite depth and possesses a constant vorticity.

There has been much interest in the calculation of bow or stern flows in recent years with particular interest given to the question of whether or not waveless bow flows exist. The first full nonlinear solution for the infinite-depth problem was found by Vanden-Broeck & Tuck (1977) and Vanden-Broeck, Schwartz & Tuck (1978), who summed an everywhere-divergent series using analytic continuation methods to find waves behind a rectangular shaped stern. They assumed that the free surface attached to the body at a stagnation point, and showed that solutions exist for small Froude numbers. Their Froude number is based on the draught of the ship, which is the only physical length scale for bow flows in infinitely deep water. They were unable to find solutions without waves and hence could not find any bow flows. A similar problem was considered by Vanden-Broeck (1980), where it was assumed that the fluid separated smoothly from the stern of a ship. Here stern flows were shown to exist for all draught-based Froude numbers $F_d > 2.23$.

Stern flows with stagnant detachment that exhibit no waves were found by Madurasinghe (1988). These solutions were obtained by forcing the free surface to be waveless and solving for the body shape. Since the radiation condition downstream is satisfied, such a flow can be reversed to yield a bow flow. These results, however, were disputed by Farrow & Tuck (1995), who showed that solutions corresponding to the bow shapes derived by Madurasinghe possessed very small waves. In fact, they claim that the solutions found by Madurasinghe were simply in a parameter region where very small waves are always present, regardless of the body shape. For the case where the free surface attaches to the body smoothly, waveless solutions were found by both Madurasinghe & Tuck (1986) and Farrow & Tuck (1995).

† Present address: Division of Theoretical Mechanics, School of Mathematical Sciences, University of Nottingham, University Park, Nottingham NG7 2RD, UK.

Related problems where the fluid is of finite depth have been considered by Vanden-Broeck (1989) and Hocking (1993). Vanden-Broeck showed that there exist bow flows in front of a rectangular body with stagnant attachment. A unique solution was found for all Froude numbers between 1.22 and $\sqrt{2}$, where this time the Froude number is based on the depth of the fluid upstream. Hocking found waveless solutions for all values of Froude number $F > 1$ when the fluid attached to the front of an inclined bow smoothly. No stern flows in a fluid of finite depth have been documented.

When waveless bow flows do not exist it is conjectured that other sorts of flows may be present, such as ones that meet the body with a splash. Some of these splashing flows have been calculated by Dias & Vanden-Broeck (1993), and more recently by Tuck, Simakov & Wiryanto (1997).

All of the above research has been conducted for the case where the flow is irrotational. The purpose of this study is to consider the case when the flow is not irrotational but possesses a constant vorticity throughout. We consider the flow past a bow-shaped object in a fluid of finite depth. The problem is solved using a boundary integral method in the physical plane for the case where the free surface meets the body at a stagnation point. Physically, such a flow might be associated with a barge travelling up a shallow river, where the constant shear flow upstream has been created by a bottom boundary layer. Alternatively, this model could be used to describe the flow of fluid into a horizontal slot. In this case, wind could be the mechanism that is driving the shear flow.

Waveless bow flows are shown to exist for supercritical Froude numbers. Here the Froude number is an unknown and has to be found as part of the solution process. It is shown that for most values of the vorticity, the solutions are qualitatively similar to those for the irrotational flow past a rectangular body (see Vanden-Broeck 1989).

Subcritical solutions are also found. These solutions are characterized by a train of waves in front of the body. Since the radiation condition is not satisfied, these solutions must describe the flow past the stern of a body and cannot be classified as bow flows. We show that the amplitude of these stern waves increases both with increasing Froude number and vorticity, and also increases as the body penetration into the fluid (the draught) decreases.

2. Supercritical stagnation point flow

2.1. *Mathematical formulation*

We consider the steady flow of an inviscid fluid past a semi-infinite rectangular body with a rounded corner, as shown in figure 1. The rounded corner is to avoid the singular behaviour that occurs with inviscid fluids near a rectangular corner, where the velocity becomes infinite. The flow is rotational, with constant vorticity ω, and approaches a uniform shear flow upstream with speed c on the bottom and speed $c+\omega H$ on the free surface. The distance of the body from the bottom and the radius of the quarter-circle at the body corner are denoted by D and R respectively.

Cartesian coordinates are introduced so that the x-axis lies on the bottom and the y-axis points vertically upwards. The vertical face of the body is located at $x = 0$. We non-dimensionalize all lengths and speeds with respect to the upstream height H and upstream bottom speed c. It follows that the problem now depends on the four parameters

$$F = \frac{c}{\sqrt{gH}}, \quad \Omega = \frac{\omega H}{c}, \quad \gamma = \frac{D}{H}, \quad \alpha = \frac{R}{H}. \tag{2.1}$$

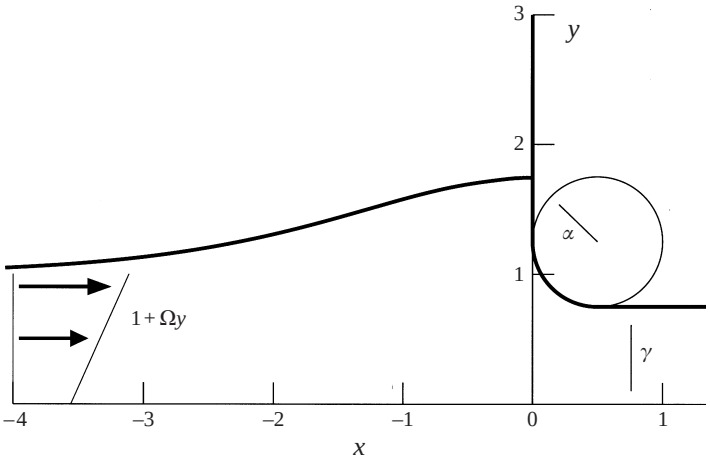

FIGURE 1. A diagram of free surface flow in non-dimensional variables caused by an immersed body, in the presence of constant vorticity Ω. The radius α of the curved body nose is indicated. The free surface profile is taken from an actual solution with $F = 1.22$, $\Omega = 0$, $\gamma = 0.75$ and $\alpha = 0.5$. The scale on both axes is the same.

Here F is the Froude number, which is a measure of the fluid speed upstream when there is no vorticity. The parameter Ω is simply the dimensionless vorticity while the parameters γ and α are the dimensionless gap height and circle radius respectively. The constant g is the acceleration due to gravity.

Since the fluid is incompressible and the flow is rotational, it can be described by the non-dimensional streamfunction $\psi(x, y)$ that satisfies the equation

$$\nabla^2\psi = \Omega, \tag{2.2}$$

throughout the flow region. We see that if we write

$$\psi(x, y) = y + \tfrac{1}{2}\Omega y^2 + \Psi(x, y), \tag{2.3}$$

then the pseudostreamfunction Ψ satisfies Laplace's equation. It follows that there exists a pseudovelocity potential $\Phi(x, y)$ such that the x and y components of the velocity vector can be expressed as

$$u(x, y) = 1 + \Omega y + U(x, y), \qquad v(x, y) = V(x, y), \tag{2.4}$$

where

$$U = \frac{\partial\Psi}{\partial y} = \frac{\partial\Phi}{\partial x}, \qquad V = -\frac{\partial\Psi}{\partial x} = \frac{\partial\Phi}{\partial y}. \tag{2.5}$$

At this stage it is convenient to parametrize the free surface and body with respect to an arclength s. We set $s = 0$ at the stagnation point so that $s \to -\infty$ far upstream on the free surface and $s \to \infty$ far downstream on the body. All points on the free surface and body can now be written as $(x(s), y(s))$ where $x(s)$ and $y(s)$ satisfy the arclength condition

$$x'(s)^2 + y'(s)^2 = 1. \tag{2.6}$$

The use of the above parametrization and the following integral equation method has become quite common recently, and some examples can be found in Forbes (1985), Forbes & Belward (1996) and Vanden-Broeck (1994).

It can be seen from (2.5) that the quantity $f(z) = \Phi + \mathrm{i}\Psi$ is an analytic function of $z = x + \mathrm{i}y$ in the flow domain. This implies that the quantity $\chi(z) = U - \mathrm{i}V$ is also an

analytic function within the fluid, and vanishes far upstream. Consider the curve Γ which consists of the free surface and body, except the fixed point $(x(s), y(s))$ which is by-passed by a semicircle of vanishingly small radius, the image free surface and body obtained by reflecting the fluid region about the bottom, and two vertical lines at $x = \pm\infty$ connecting the fluid surface and its image. The application of Cauchy's integral formula to χ around this curve yields the integral equation

$$\oint_{\Gamma} \frac{\chi(z(t))z'(t)}{z(t) - z(s)}\mathrm{d}t = 0. \tag{2.7}$$

Notice that the act of reflecting the flow across the x-axis enforces the kinematic condition $V = 0$ on the bottom.

The contribution to the integral in (2.7) from the vertical line at $x = -\infty$ is clearly zero since both U and V vanish upstream. To evaluate the contribution from the vertical line at $x = \infty$, we consider the integral over a shifted vertical line situated far downstream at $x = d$, and let $d \to \infty$. Here, the vertical velocity V vanishes but the horizontal velocity U approaches some constant value $\overline{U}$ given by

$$\overline{U} = [(1 + \Omega/2) - (\gamma + \Omega\gamma^2/2)]/\gamma, \tag{2.8}$$

which can be found by considering conservation of mass. It is straightforward to show that the integral over this vertical line is

$$\overline{U}\arctan\left(\frac{\gamma + y(s)}{d - x(s)}\right) + \overline{U}\arctan\left(\frac{\gamma - y(s)}{d - x(s)}\right) + \overline{U}\ln\left[\frac{(d - x(s))^2 + (\gamma + y(s))^2}{(d - x(s))^2 + (\gamma - y(s))^2}\right]^{1/2},$$

and that as $d \to \infty$, this contribution also vanishes.

By making use of the reflection conditions, we can show that the imaginary part of what is left in equation (2.7) eventually yields the required integral equation

$$\pi U(s) = \fint_{-\infty}^{\infty} \frac{\Phi'(t)(y(t) - y(s)) - \Psi'(t)(x(t) - x(s))}{(x(t) - x(s))^2 + (y(t) - y(s))^2}\mathrm{d}t + \int_{-\infty}^{\infty} \frac{\Phi'(t)(y(t) + y(s)) - \Psi'(t)(x(t) - x(s))}{(x(t) - x(s))^2 + (y(t) + y(s))^2}\mathrm{d}t, \tag{2.9}$$

where $\Phi'(t) = U(t)\,x'(t) + V(t)\,y'(t)$ and $\Psi'(t) = -V(t)\,x'(t) + U(t)\,y'(t)$. The bar through the first integral sign indicates that the integral is to be interpreted in the Cauchy Principal Value sense.

Now the condition of constant pressure on the free surface is given by Bernoulli's equation

$$\tfrac{1}{2}(1 + \Omega y + U(s))^2 + \tfrac{1}{2}V(s)^2 + \frac{1}{F^2}y(s) = \tfrac{1}{2}(1 + \Omega)^2 + \frac{1}{F^2}, \tag{2.10}$$

on this surface. The fact that the fluid cannot pass through its own boundary leads to the kinematic condition $\mathrm{d}\psi/\mathrm{d}s = 0$ on the free surface and body. This condition can be expressed, using (2.3), in the form

$$\Psi'(s) = -(1 + \Omega y(s))\,y'(s), \tag{2.11}$$

for all s.

It is seen from (2.10) that the height of the stagnation point, denoted by y_a, is given by

$$y_a = \frac{F^2}{2}(1 + \Omega)^2 + 1, \tag{2.12}$$

since the velocities u and v in equation (2.4) vanish at this point. We let $s = s_b =$

$y_a - (\gamma + \alpha)$ at the top of the quarter-circle and $s = s_c = s_b + \pi\alpha/2$ at the bottom of the quarter-circle so that the body can be described by

$$x(s) = \begin{cases} 0, & 0 \leqslant s \leqslant s_b \\ \alpha[1 - \cos((s - s_b)/\alpha)], & s_b \leqslant s \leqslant s_c \\ s - s_c + \alpha, & s \geqslant s_c, \end{cases} \tag{2.13}$$

and

$$y(s) = \begin{cases} y_a - s, & 0 \leqslant s \leqslant s_b \\ \gamma + \alpha[1 - \sin((s - s_b)/\alpha)], & s_b \leqslant s \leqslant s_c \\ \gamma, & s \geqslant s_c. \end{cases} \tag{2.14}$$

The problem is now reduced to finding the functions $x(s)$, $y(s)$, $U(s)$ and $V(s)$ such that equations (2.9)–(2.11) and (2.13)–(2.14) are satisfied. The numerical method used to do this is described in § 2.2.

We briefly now consider some results that can be found from linear theory. The linear dispersion relation for gravity waves with constant vorticity ω is

$$\tanh kH = \frac{k(c + \omega H)^2}{\omega(c + \omega H) + g}, \tag{2.15}$$

where k is the wavenumber. This equation has real solutions for k when

$$\frac{(c + \omega H)^2}{\omega H(c + \omega H) + gH} < 1,$$

or in our non-dimensional variables, when

$$F^2 < \frac{1}{1 + \Omega}.$$

Therefore linear theory tells us that the critical Froude number is

$$F_c = \frac{1}{\sqrt{1 + \Omega}}, \tag{2.16}$$

and that small-amplitude waves can only exist if $F < F_c$.

Using the dispersion relation (2.15), the group velocity of any such linear waves can be evaluated to give

$$\begin{aligned} c_g = \frac{\mathrm{d}}{\mathrm{d}k}(kc_p) &= c_p \left[\left(1 + \frac{2kH}{\sinh 2kH} \right) \frac{g}{\omega c_p + 2g} + \frac{\omega c_p}{\omega c_p + 2g} \right] \\ &= c_p \left[\left(1 + \frac{2kH}{\sinh 2kH} \right) \frac{1}{F^2\Omega(1 + \Omega) + 2} + \frac{F^2\Omega(1 + \Omega)}{F^2\Omega(1 + \Omega) + 2} \right], \end{aligned}$$

where c_p is the phase velocity given by $c_p = c + \omega H$. Using the inequality

$$1 < 1 + \frac{2kH}{\sinh 2kH} < 2,$$

and the fact that we restrict ourselves to vorticity values $\Omega > -1$, it can easily be shown that the group velocity c_g is always less than the phase velocity c_p. It follows from this result that steady waves, at least of small amplitude, cannot propagate ahead of a body moving at a constant velocity. This result is well known for irrotational flows, and is known as the radiation condition.

It should be noted that for finite-amplitude waves, the linear theory described above

is no longer valid and in fact steady waves can be found for Froude numbers greater than the critical value F_c. For example, when $\Omega = 0$, Cokelet (1977), Vanden-Broeck & Schwartz (1979) and others have accurately calculated periodic, steady waves on the surface of a finite-depth fluid for Froude numbers up to about 1.29.

2.2. *Numerical method*

We place a mesh of N equally spaced grid points $s_1, s_2, \ldots, s_{na}, \ldots, s_N$ over the free surface and body so that the points s_1 and s_N approximate $-\infty$ and ∞ respectively. The point $s_{na} = 0$ is the stagnation point and we choose $na = (N+1)/2$. Care has to be taken at this point since the quantities $x'(s)$ and $y'(s)$ are discontinuous here. It is therefore convenient to make the point s_{na} a double point so that $x'_{na^-} = 1$, $y'_{na^-} = 0$, $x'_{na^+} = 0$ and $y'_{na^+} = -1$.

For a given set of values for the parameters γ, Ω and α, it is expected that the Froude number will be an unknown that has to be found as a part of the solution process, as was the case in the similar problem considered by Vanden-Broeck (1989). We therefore include F in our vector of $(3N-1)/2$ unknowns

$$\boldsymbol{u} = [y'_1, \ldots, y'_{na-1}; \Phi'_1, \ldots, \Phi'_{na-1}, \Phi'_{na+1}, \ldots, \Phi'_N; F]^T.$$

Newton's method is used to solve for this vector by forcing an error vector $\boldsymbol{E}(\boldsymbol{u})$ to zero.

Given an initial guess for $\boldsymbol{u}$, all the flow quantities are known or can be easily calculated. The x'_i can be found from the arclength condition (2.6), while the Ψ'_i can be found from the kinematic condition (2.11). A backward trapezoidal rule can be used to find all the x_i and y_i on the free surface, given that $x_{na} = 0$ and $y_{na} = 1 + F^2(1+\Omega)^2/2$. That is,

$$x_{na-j} = x_{na+1-j} - (s_{na+1-j} - s_{na-j})(x'_{na+1-j} + x'_{na-j})/2,$$
$$y_{na-j} = y_{na+1-j} - (s_{na+1-j} - s_{na-j})(y'_{na+1-j} + y'_{na-j})/2,$$

for $j = 1 \ldots na-1$. Finally, the x_i, y_i, x'_i and y'_i on the body can be simply found from (2.13)–(2.14), and the velocities U_i and V_i can be found from

$$U(s) = x'(s)\,\Phi'(s) + y'(s)\,\Psi'(s),$$
$$V(s) = y'(s)\,\Phi'(s) - x'(s)\,\Psi'(s).$$

The error vector $\boldsymbol{E}(\boldsymbol{u})$ consists of the following $(3N-1)/2$ components. The first $N-1$ components are obtained from evaluating the integral equation (2.9) at the $N-1$ half-mesh points $s_{j+1/2}$, $j = 1, \ldots, N-1$. The integrals in (2.9) are approximated using the trapezoidal rule and the singularity can be ignored since we have taken $s_{j+1/2}$ to lie halfway between the mesh points. Linear interpolation is used to calculate the function values $x_{j+1/2}$, $y_{j+1/2}$ and $U_{j+1/2}$ at these half-mesh points.

Since $U(s)$ does not vanish as $s \to \infty$, it is necessary to estimate the contributions to the integrals in equation (2.9) from the region $s > s_N$ that is ignored in the numerical method. These truncation terms can be found by making the assumptions

$$x(s) = x_N + (s - s_N), \quad y(s) = \gamma, \quad U(s) = \overline{U}, \quad V(s) = 0,$$

far downstream, for $s > s_N$. Here $\overline{U}$ is given by equation (2.8). With these assumptions, the portion of the integrals in (2.9) from s_N to ∞ can be evaluated directly to give

$$\overline{U} \arctan\left(\frac{\gamma + y(s)}{x_N - x(s)}\right) + \overline{U} \arctan\left(\frac{\gamma - y(s)}{x_N - x(s)}\right).$$

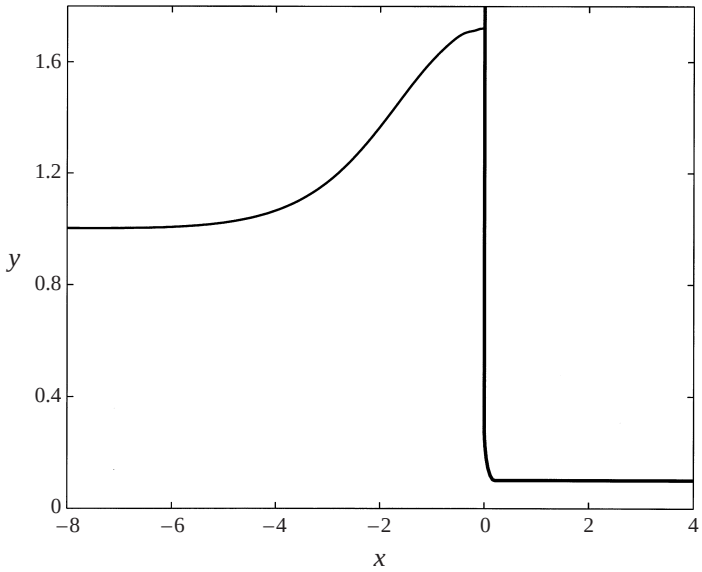

FIGURE 2. Typical free surface profile for $F > 1/\sqrt{1+\Omega}$. Here $F = 1.20$, $\Omega = 0$, $\gamma = 0.1$ and $\alpha = 0.2$.

These truncation terms are included in the first $N-1$ components of the error vector. It should also be noted that since $x'(s)$ and $y'(s)$ are discontinuous at $s = 0$ then the integrals have to be split into two parts, the first for $s_1 \leqslant t \leqslant 0$ and the second for $0 \leqslant t \leqslant s_N$.

The next $na-1$ components of $\boldsymbol{E}$ come from evaluating Bernoulli's equation (2.10) at the points $s_1, \ldots, s_{na-1}$. Finally, the last component enforces the radiation condition $y_1' = 0$ upstream.

2.3. *Results*

The numerical scheme given in the last subsection was used to compute many solutions for different values of γ, Ω and α. It has been found that results are obtained that are acceptably insensitive to the numerical discretization, provided that at least $N = 401$ mesh points are used over an interval within $s_1 = -10$ and $s_N = 10$. (We illustrate this point later by providing an example of a free surface profile computed using different grid spacings). Results in this section are therefore presented using this numerical grid spacing and number of points, unless stated otherwise.

A typical free surface profile obtained with this method is presented in figure 2. For this solution the vorticity $\Omega = 0$ and the Froude number $F = 1.20$. The body face lies along a portion of the line $x = 0$, and the bottom is at the height $\gamma = 0.1$. These two sections of the body are connected by the circular portion of radius $\alpha = 0.2$, which forms the smooth corner at the bottom of the bow. In this figure and subsequent similar figures, this circular portion is barely noticeable as the radius α is relatively small and the range of x values is much greater then the range of y values. The free surface is the portion ahead of the bow, in the fluid region $x < 0$. Far ahead of the body, for $x \to -\infty$, the surface is asymptotically flat, and rises to the stagnation height y_a given by equation (2.12), at the point at $x = 0$ where the surface intersects the body.

As the circle radius $\alpha \to 0$, the flow considered in this section approaches that past

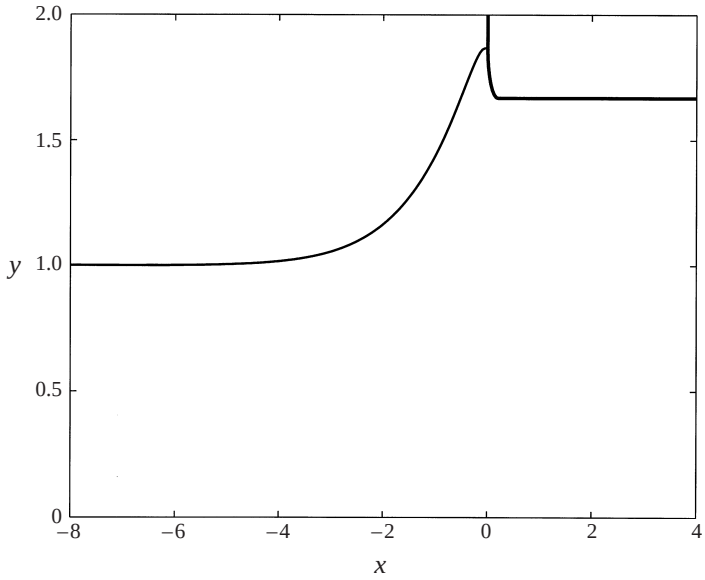

FIGURE 3. Free surface profile for the limiting case where the height of the attachment point $y_a = \gamma + \alpha$. Here $F = 1.32$, $\Omega = 0$, $\gamma = 1.67$ and $\alpha = 0.2$.

a semi-infinite rectangular body. This geometry was considered by Vanden-Broeck (1989) for the case where the flow is irrotational ($\Omega = 0$). Our numerical method cannot deal with this limiting configuration exactly, because of the need to place grid points on the quarter-circular portion of the bow; however the irrotational results for non-zero α were found to be qualitatively the same as those found by Vanden-Broeck. The reliability of the method deteriorated for small radii and it was found that more than $N = 401$ grid points were needed when the radius was less than about $\alpha = 0.05$.

Figure 2 represents an irrotational solution at close to the smallest value of the gap height γ between the bottom and the body for which the numerical scheme of § 2.2 gives results of reliable accuracy. For smaller values of γ, the very high fluid speeds generated in the region $x > 0$ erode the accuracy of the method. In the limit $\gamma \to 0$, the flow becomes equivalent to that for a line sink situated in a corner at $(x, y) = (0, 0)$, at least if the circle radius $\alpha \to 0$. This configuration was considered by Mekias & Vanden-Broeck (1989), who showed that the limiting Froude number for this case is expected to be $F = 1.22$. Our numerical method is not capable of calculating this solution but it is clear that for small γ and α the resulting free surface is very similar to that found by Mekias & Vanden-Broeck, as can be seen by figure 2.

As the gap height γ increases, irrotational solutions can be found until the top of the circular portion of the bow rises to the height of the attachment point, so that $y_a = \gamma + \alpha$. Such a solution is shown in figure 3. Numerically, this is our limiting solution, as we have restricted ourselves to the case where the free surface meets the bow on the front face only. However, physically, if γ is increased even further, the free surface will attach horizontally to the quarter-circular portion of the bow. This will happen until $y_a = \gamma + \alpha/2$, at which point the free surface is attaching at an angle of 120° to the body. Then as γ continues to increase, the angle of attachment remains at 120°, as indicated by Dagan & Tulin (1972). Finally, the limiting configuration in the physical sense is ultimately reached when the height of the attachment point y_a is equal to the gap height γ. This critical configuration has been considered by

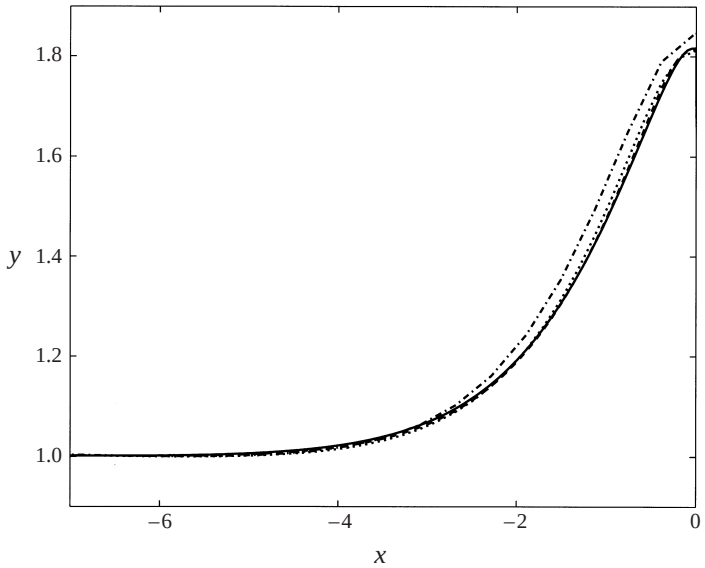

FIGURE 4. Free surface profiles for $\Omega = 0$, $\gamma = 1.5$ and $\alpha = 0.2$ computed on four different grids. The dot-dashed, dotted, dashed and solid lines correspond to solutions computed with $N = 51$, 101, 201 and 401 mesh points respectively. The computed Froude number is $F = 1.30$ when $N = 51$ and $F = 1.28$ when $N = 101$, 201 and 401.

Vanden-Broeck (1989) and is also the limiting case for the flow of an irrotational fluid under a semi-infinite plate (see Asavanant & Vanden-Broeck 1996; Benjamin 1968; and Vanden-Broeck & Keller 1987). Both Benjamin and Vanden-Broeck & Keller show analytically that $F = \sqrt{2}$ and $\gamma = 2$ for this flow. We have also computed this solution using a similar boundary integral method to the one used in this section, and the details will be given elsewhere (McCue & Forbes 1999).

The convergence behaviour of our numerical method can be monitored graphically by comparing free surface profiles computed with the same parameter values, but with different numbers of grid points N. For example, figure 4 contains four free surface profiles for the case where $\gamma = 1.5$, $\Omega = 0$ and $\alpha = 0.2$. The dot-dashed, dotted, dashed and solid profiles are calculated with $N = 51$, 101, 201 and 401 grid points respectively. It can be seen that the shape of the profile for $N = 51$ is significantly different from the other three. There is a slight difference between the solution profile for $N = 101$ and the profile for $N = 201$, but the solution profiles for $N = 201$ and $N = 401$ are very close together. All solutions calculated with more than $N = 401$ grid points have free surface profiles that essentially lie directly on top of the solid profile. The computed Froude number here is $F = 1.30$ for $N = 51$ and $F = 1.28$ for the other three grids.

A large number of solutions has been generated for various circle radii ranging from $\alpha = 0.05$ to about $\alpha = 1.0$, and it has been shown that varying this parameter has no qualitative effect on the results found. We therefore fix $\alpha = 0.2$ for the rest of this section and investigate the effect that vorticity has on our solutions.

With the radius of the curved section of the bow fixed at $\alpha = 0.2$, it is found that for all $-0.76 < \Omega < 0.33$ the nature of the solutions is similar to that found for $\Omega = 0$. That is, solutions can be found for arbitrary values of the bow height γ until $y_a = \gamma + \alpha$ is achieved at the limiting configuration. Figure 5(*a*) shows the relationship between the Froude number F and the bow height γ for different values

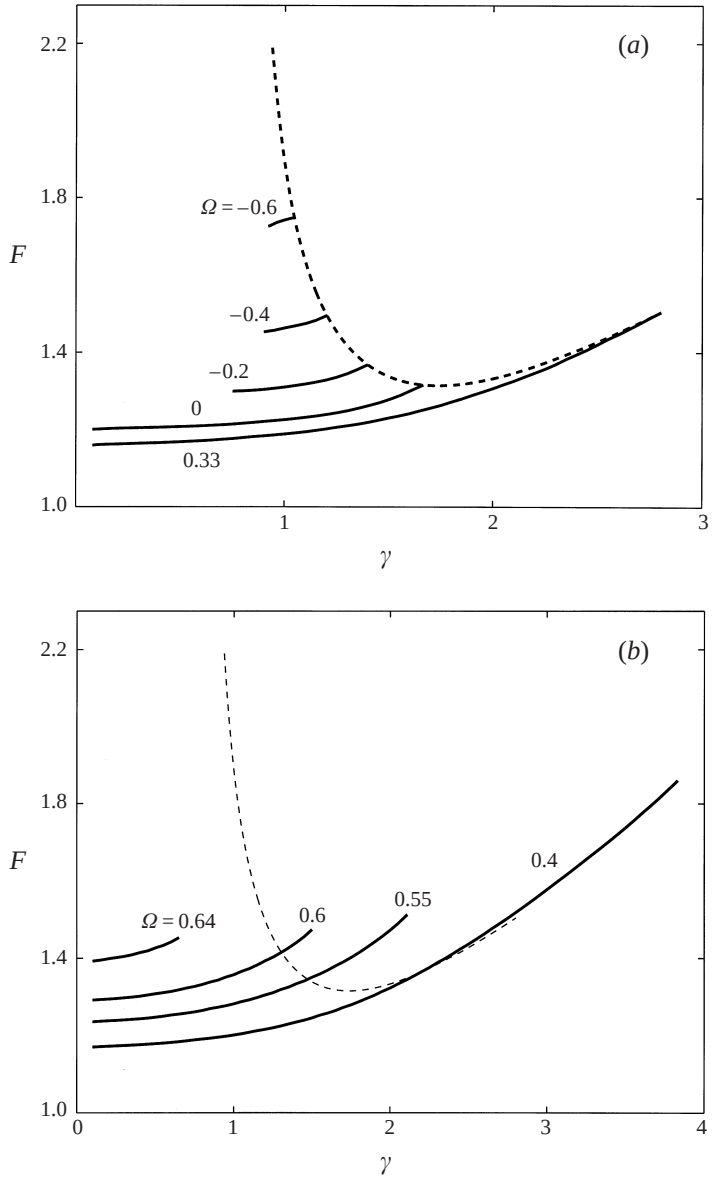

FIGURE 5. The dependence of the Froude number F on the gap height γ for nine different values of the vorticity. In (a) the curves corresponding to $\Omega = -0.6$, -0.4, -0.2, 0 and 0.33 terminate at the dashed curve. This curve indicates the limiting case solutions where the height of the attachment point $y_a = \gamma + \alpha$. In (b), the curves corresponding to $\Omega = 0.4$, 0.55, 0.6 and 0.64 do not terminate at the dashed curve, however this curve is included for reference. All solutions are found for $\alpha = 0.2$.

of the vorticity Ω in this range. It can be seen that for $\Omega = 0$ and 0.33, accurate solutions could be obtained for all gap heights down to about $\gamma = 0.08$. Beyond this value it was found that the high fluid speeds under the body caused the results to become unreliable. Solutions for vorticity values $\Omega = -0.6$, -0.4 and -0.2, however, could not be found for all gap heights γ below their limiting value. Instead, it was found that at some γ the surface profiles began to exhibit small spurious waves near

the stagnation point. These numerical artifacts were found to exist only in a small interval of values of γ, after which no solutions could be computed.

Included in figure 5(*a*), sketched with a dashed line, is a plot of F versus γ for the limiting case, at which the interface meets the body at the top of the circular portion of the bow, as in figure 3. Solutions for the limiting case were found using the numerical method described in § 2.2 with an extra unknown, γ, and an extra component of the error vector that enforces the condition $y_a = \gamma + \alpha$. Solutions for this limiting configuration just below and including $\Omega = 0.33$ converged slowly using a previously calculated solution with similar Ω as an initial guess, while no such solutions could be found for $\Omega > 0.33$. The behaviour of the convergence of these solutions is different for values of the vorticity Ω near -0.76. Highly converged solutions could be obtained for Ω just greater and just less than -0.76, but -0.76 is the lowest vorticity for which a limiting case solution was obtained with a smooth free surface profile. For values of $\Omega < -0.76$, the only limiting case solutions found contained spurious waves near the stagnation point and hence are not included in this plot. This figure should be viewed in conjuction with figure 7, which will be discussed later.

When the vorticity is fixed at values greater than 0.33, the nature of the solutions changes. Numerically, solutions can be found by gradually increasing γ and using the previously calculated solution as the initial guess, as done with the critical solutions described above. However, a limiting case solution where $y_a = \gamma + \alpha$ is never reached. Instead, a maximum γ value was found above which the numerical scheme failed to converge. The reason for this failure is not readily apparent.

This behaviour is illustrated in figure 5(*b*), where the relationship between the Froude number F and the gap height γ is shown for vorticity values $\Omega = 0.4$, 0.55, 0.6 and 0.64. Also shown in figure 5(*b*) is the dotted curve taken from figure 5(*a*). This curve represents limiting case solutions for $-0.76 < \Omega < 0.33$. It is not applicable for vorticity values $\Omega > 0.33$ and is intended for reference only.

As indicated above, the solutions in figure 5(*b*) fail abruptly at some limiting value of the gap height γ, for each $\Omega > 0.33$. Unlike the results in figure 5(*a*), there is now no obvious physical explanation for the termination of these curves, and a comparison of the solution at the maximum possible value of γ with one obtained with a smaller γ, for fixed vorticity Ω, reveals no qualitative difference. It was at first thought that the curves in figure 5(*b*) might undergo a fold bifurcation at the maximum point, but subsequent careful numerical checking indicates this is apparently not the case. There is thus no present physical explanation for the abrupt failure of the solution curves in figure 5(*b*). An analogous situation exists for the free surface flow with a stagnation point due to a line sink, where Hocking & Forbes (1991) similarly found a solution branch that terminated without obvious physical cause. Forbes & Hocking (1993) later suggested that a degenerate fold singularity might be present at the limiting case, and perhaps the same behaviour occurs here also. We note here that since the attachment height y_a is proportional to F^2, a plot of y_a versus γ for fixed vorticity Ω would produce similar behaviour to the corresponding plot in figure 5.

We now consider the effect that varying the vorticity Ω has on the flow when the gap height γ is fixed. Figures 6(*a*) and 6(*b*) show different free surface profiles for $\gamma = 0.75$ and $\gamma = 1.5$. In each case, the largest value of the vorticity ($\Omega = 0.63$ for $\gamma = 0.75$ and $\Omega = 0.6$ for $\gamma = 1.5$) corresponds to the last solution found before the iteration scheme failed to converge. The surface profile in figure 6(*a*) for $\Omega = -0.2$ corresponds to the solution for fixed $\gamma = 0.75$ with the lowest vorticity obtainable before the smoothness of the free surface breaks down. Numerical solutions with

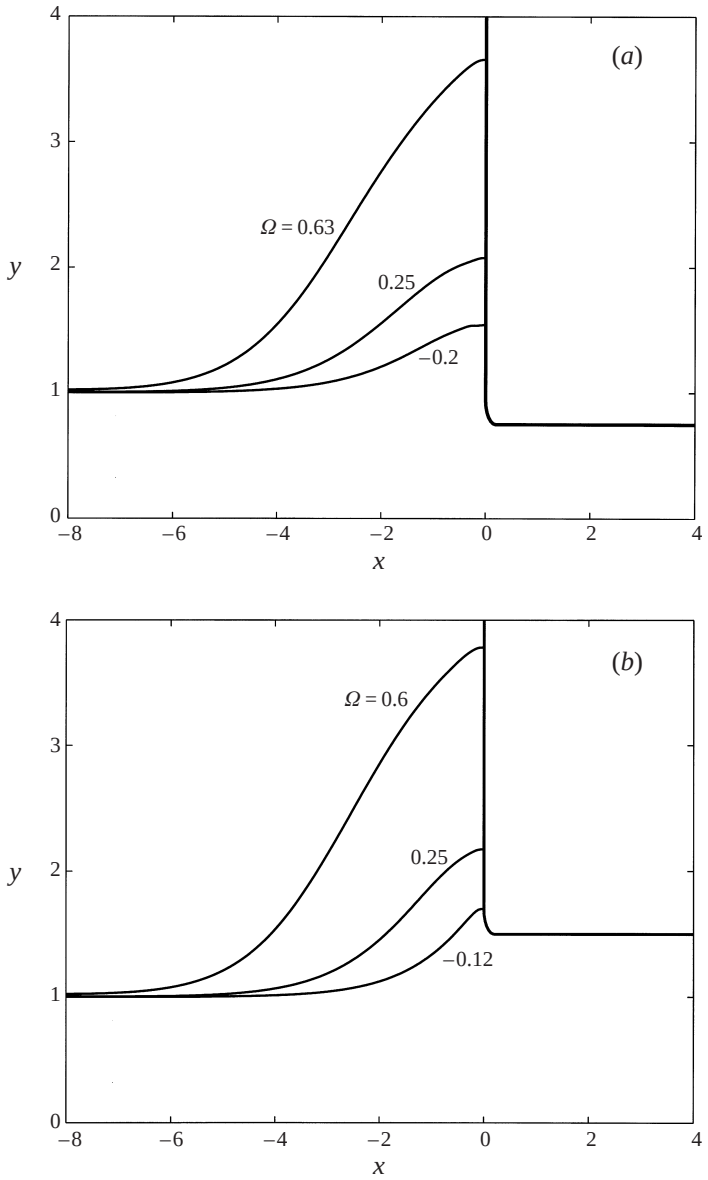

FIGURE 6. Typical free surface profiles for (*a*) $\gamma = 0.75$ and (*b*) $\gamma = 1.5$. For $\gamma = 0.75$, the profiles from top to bottom are found for vorticity values $\Omega = 0.63$, 0.25 and -0.2 and the corresponding calculated Froude numbers are $F = 1.41$, 1.17 and 1.30. For $\gamma = 1.5$, the profiles from top to bottom are found for vorticity values $\Omega = 0.6$, 0.25 and -0.12 and the corresponding calculated Froude numbers are $F = 1.47$, 1.23 and 1.34. All solutions are found for circle radius $\alpha = 0.2$.

this gap height for Ω less than -0.2 could be found; however the corresponding free surface profiles showed small spurious waves near the stagnation point and hence are not reliable. On the other hand, when $\gamma = 1.5$ as in figure 6(*b*), the solution with the lowest vorticity Ω is the limiting case where the stagnation point height $y_a = \gamma + \alpha$. In fact for all fixed gap heights $\gamma \geqslant 0.94$, the lowest Ω obtainable is when the solution coincides with this critical configuration.

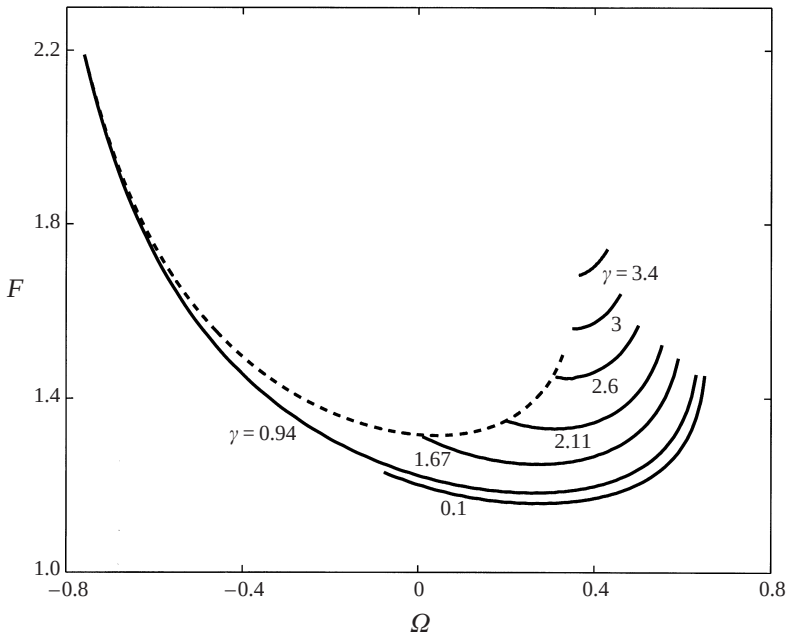

FIGURE 7. The dependence of the Froude number F on the vorticity Ω for seven different values of the gap height $\gamma = 0.1$, 0.94, 1.67, 2.11, 2.6, 3 and 3.4. The dashed line indicates the limiting case solutions where the height of the attachment point $y_a = \gamma + \alpha$. All solutions are found for $\alpha = 0.2$.

Five plots of the Froude number F versus the vorticity Ω for different gap heights γ are shown in figure 7. The curves from bottom to top correspond to $\gamma = 0.1$, 0.94, 1.67, 2.11, 2.6, 3 and 3.4. In each case, the curves terminate at some positive vorticity for reasons which are not apparent at this stage. Included in figure 7 is a plot of F versus Ω for the limiting case described earlier, where the stagnation point on the body occurs at the height $y_a = \gamma + \alpha$. This is sketched with a dashed line. As expected, we see that for the biggest six gap heights γ, the corresponding plots touch this limiting curve at each lowest possible vorticity value. We also see that for the gap height fixed at $\gamma = 0.1$, the corresponding plot does not touch the limiting curve as there is no limiting case solution for any $\gamma < 0.94$. Instead, the plot for $\gamma = 0.1$ terminates at its left-hand side at the transition point where solutions begin to exhibit small spurious waves near the stagnation point. These unreliable solutions were found to exist only for a small interval of vorticity values, after which the numerical scheme would not converge at all.

No obvious physical explanation exists for the abrupt termination of the curves on the right-hand side of figure 7, as described previously in relation to figure 5(*b*). Although the curve for $\gamma = 0.1$, in particular, becomes nearly vertical at the limiting value of Ω, careful numerical checking indicates that a fold bifurcation apparently does not occur there.

3. Subcritical stagnation point flow

3.1. *Numerical method*

As stated in the last section, no subcritical solutions were found when the Froude number was assumed to be an unknown of the problem. However, when F was fixed

and the radiation condition ($y_1' = 0$) dropped, it was found that there exist solutions for $F < 1/\sqrt{1+\Omega}$ characterized by a train of waves in front of the body. Here we describe the altered numerical method used to calculate these flows. This method is essentially the same as before, except that the number of unknowns and equations is reduced by one.

Again we have rotational flow where the x and y components of the velocity vector can be written as in (2.4); however now it is not assumed that the velocities U and V vanish upstream. Following the formulation in § 2.1 we obtain the same integral equation (2.9), with the same conditions (2.6), (2.10)–(2.14). A new vector of $(3N-3)/2$ unknowns

$$\boldsymbol{u} = [y_1', \ldots, y_{na-1}'; \Phi_1', \ldots, \Phi_{na-1}', \Phi_{na+1}', \ldots, \Phi_N']^T$$

is defined and, as before, Newton's method is used to solve for this vector by forcing an error vector $\boldsymbol{E}(\boldsymbol{u})$ to zero. The first $N-1$ components of this new error vector again can be found by evaluating the integral equation (2.9) at the $N-1$ half-grid points. The integrals are evaluated in the same manner as described before. The last $na-1$ components come from the application of the Bernoulli equation (2.10) at the points $s_1, \ldots, s_{na-1}$.

3.2. *Results*

Using the numerical method described in the last subsection we have calculated many different solutions for various values of the parameters F, γ, Ω and α. All of the solutions found were characterized by a train of waves in front of the body. Unlike the results in § 2.3, when the radiation condition was enforced, no supercritical ($F > 1/\sqrt{1+\Omega}$) solutions were found in this case.

As with the supercritical flows, it was observed that varying the bow radius α has no qualitative effect on the behaviour of the solutions. We therefore set $\alpha = 0.1$ when presenting numerical results in this section. The number of grid points and grid size used in calculating the solutions differed for each set of parameters, but at all times the results were checked so that the free surface was independent of the grid within graphical accuracy.

Typical free surface profiles for $\Omega = 0$ are shown in figures 8 and 9. Figure 8 shows that when the gap height is held constant at $\gamma = 0.4$, the amplitude and wavelength of the waves increases quite considerably as the Froude number increases. For $F = 0$ there is no flow and the free surface is flat. For $F = 0.5$, as in figure 8(a), the waves have finite amplitude and look quite sinusoidal. On the other hand, figure 8(b) shows that when the Froude number is increased to $F = 0.8$ the waves become noticeably nonlinear with sharp crests and broad troughs. It is expected that if we increase F even further then the waves will reach the Stokes limiting configuration at some Froude number, where a corner is formed at the wave crests. This corner is a stagnation point and encloses an angle of 120°. Our numerical method should be capable of calculating flows near this limiting configuration; however in practice this has not been possible, since these nonlinear solutions require a larger number of grid points on each wavelength, and this soon becomes too computationally expensive. We note here that the behaviour of the solutions for all γ was found to be similar to that for $\gamma = 0.4$, as will be explained later. This behaviour is qualitatively similar to that found by Mekias & Vanden-Broeck (1991) in their study of the subcritical flow produced by a submerged source in a fluid of finite depth.

Figure 9 shows that when the flow is irrotational ($\Omega = 0$) and the Froude number is fixed at $F = 0.5$, the amplitude of the waves increases and the wavelength decreases

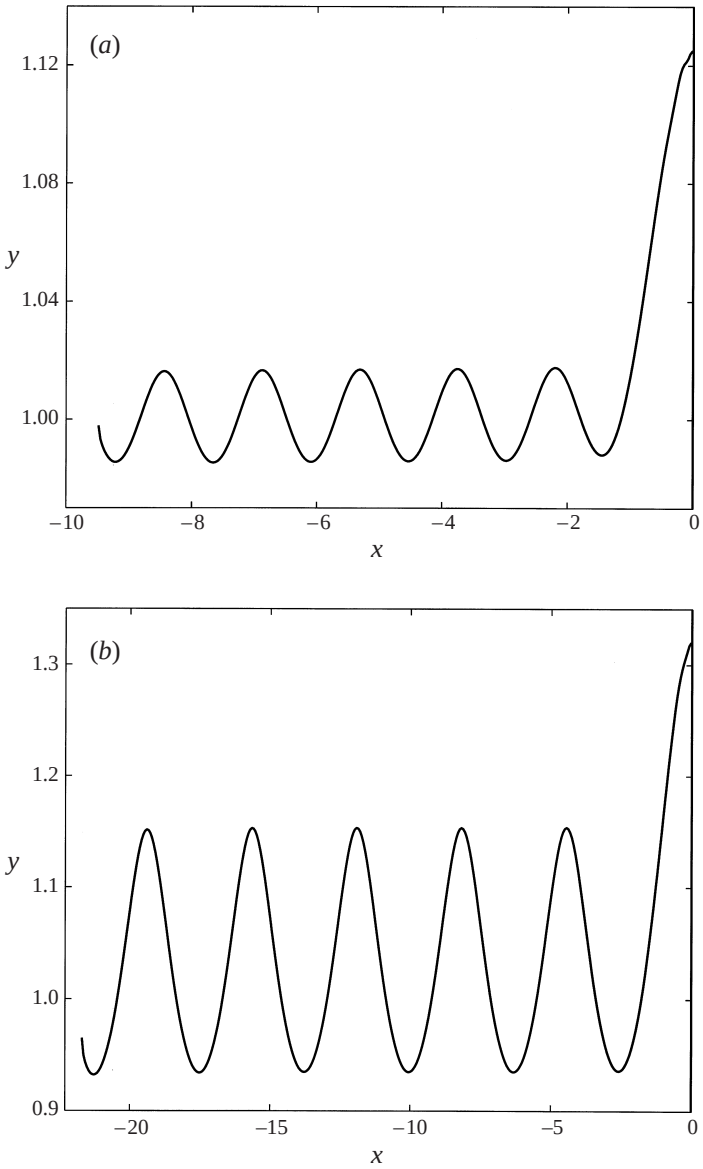

FIGURE 8. Typical free surface profiles for $\gamma = 0.4$ and $F < 1/\sqrt{1+\Omega}$. (*a*) $F = 0.5$, computed with $N = 601$ grid points, and (*b*) $F = 0.8$ computed with $N = 721$ grid points. Solutions shown are for $\Omega = 0$ and $\alpha = 0.1$.

as the height of the body above the bottom increases. This behaviour is typical and holds for all fixed F. It was found that for all Froude numbers within the range of our numerical capability, the gap height γ could be increased to unity without reaching the limiting configuration with a stagnation point at the crest of the waves. An example of this is shown in figure 9, where for $F = 0.5$, a solution exists for $\gamma = 1$. However, for a small range of large Froude numbers, the behaviour may be slightly different. Here it is expected that there will exist some $\gamma < 1$ where the nonlinear waves reach the limiting configuration. This prediction is made by analysing figure

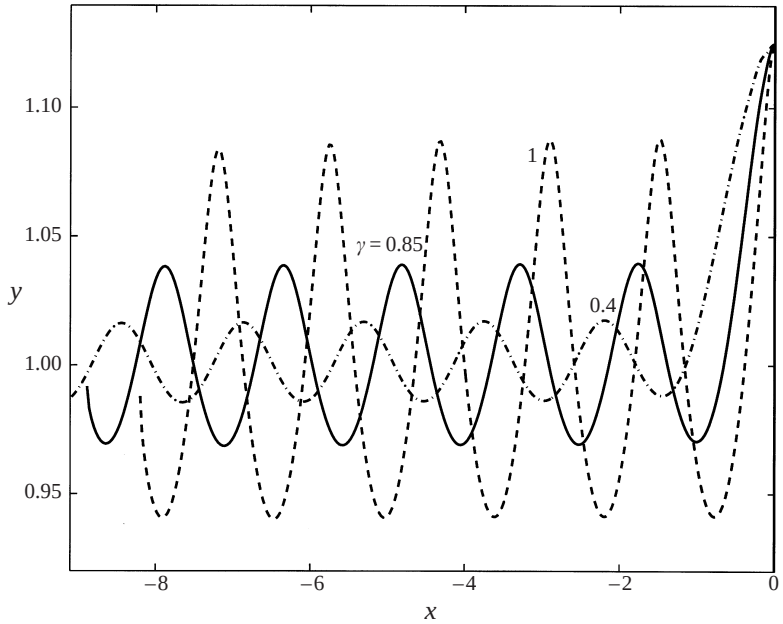

FIGURE 9. Three free surface profiles for $F = 0.5$, $\Omega = 0$ and $\alpha = 0.1$. The dot-dashed line corresponds to $\gamma = 0.4$, the solid line to $\gamma = 0.85$, and the dashed line to $\gamma = 1$. Solutions shown are computed with $N = 601$ grid points.

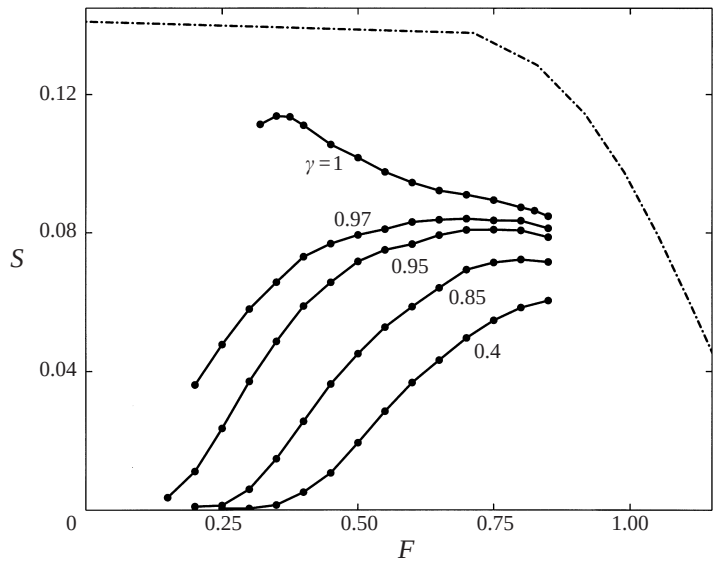

FIGURE 10. The dependence of the wave steepness S on the Froude number F for five different values of the gap height $\gamma = 0.4$, 0.85, 0.95, 0.97 and 1. Here $\Omega = 0$ and $\alpha = 0.1$. The dot-dashed line is a limiting curve, based on data from Cokelet (1977).

10, and is discussed below. It should be noted that no subcritical solutions could be found for $\gamma > 1$.

The full behaviour of solutions for $\Omega = 0$ can be neatly summarized with the aid of figure 10. In this figure, the relationship between the steepness of the upstream

waves S (defined to be the difference between the heights of the crests and the troughs divided by the wavelength) and the Froude number F is shown for gap height values $\gamma = 0.4$, 0.85, 0.95, 0.97 and 1. The number of grid points used when computing data for these curves ranged between $N = 541$ and $N = 1501$. Also shown in figure 10 is an envelope curve, sketched with a dot-dashed line, indicating the location of solutions whose waves are in the limiting configuration in which the crests enclose a 120° angle. The data for this curve have been taken from Cokelet (1977), who accurately calculated nonlinear Stokes waves using a perturbation expansion method. Steady irrotational waves can only exist on or inside this limiting curve. Note that these nonlinear solutions exist for Froude numbers up to $F = 1.29$, while linear solutions only exist up to $F = 1$. An excellent discussion on steady nonlinear water waves can be found in Schwartz & Fenton (1982). Although our calculations have only been performed up to a Froude number of $F = 0.85$, it seems clear that eventually all the curves for fixed γ will reach the limiting curve at an appropriate Froude number. Also, it seems reasonable to assume that the curve for $\gamma = 1$ will reach the limiting curve at the smallest value of F, so that for a small range of large Froude numbers, there will be solutions exhibiting the limiting configuration for values of $\gamma < 1$.

As the Froude number F decreases to zero, figure 10 shows that the steepness of the waves S also approaches zero, at least for $\gamma \leqslant 0.95$. In this section (unlike in § 2), we have allowed the free surface to attach to the upper half of the quarter-circular part of the body, ensuring that the free surface still attaches horizontally.

The curves for $\gamma = 0.97$ and 1 in figure 10 have been terminated at their left ends since solutions at lower Froude numbers have attachment heights y_a less than $\gamma + \alpha/2$, and hence the free surface starts to attach to the body at an angle of 120°, as shown by Dagan & Tulin (1972). We do not consider these types of solutions here.

We now consider the effect vorticity has on the flow. For each value of $\Omega > -1$ the behaviour of the solutions is similar to that for the irrotational case, where increasing either F or γ increases the amplitude of the waves upstream. Figure 11(*a*) shows three typical relationships between the Froude number F and the wave amplitude A for the gap height fixed at $\gamma = 0.4$. The plots from bottom to top correspond to vorticity values of $\Omega = -0.2$, 0 and 0.2 respectively. Computations for this figure have been performed using between $N = 601$ and $N = 1501$ mesh points. It is clear from this figure that the amplitude of the waves is negligible for small values of the Froude number and that as the Froude number increases, the amplitude increases faster for higher values of the vorticity. The point at the end of each of the three plots corresponds to the solution found with the highest Froude number obtainable. Our numerical method was not capable of finding more extreme flows but it is expected that the limiting case at which the waves contain 120° corners at the crests will be attained at an appropriate value of the Froude number F in each case.

Figure 11(*b*) shows the corresponding relationships between the wavelength λ of the upstream waves and the Froude number for gap height $\gamma = 0.4$. Here the computed data are represented by the solid circles. Also shown is the linear wavelengths, which are represented by the dashed lines. In each case, the linear wavelength is given by $2\pi/\kappa_0$, where κ_0 is the real root of the dispersion relation

$$\frac{\tanh \kappa}{\kappa} = \frac{F^2(1+\Omega)^2}{1+\Omega(1+\Omega)}.$$

Note that for small Froude numbers, the computed wavelength values essentially lie on the linear curve. However, for large Froude numbers, the nonlinear effects become

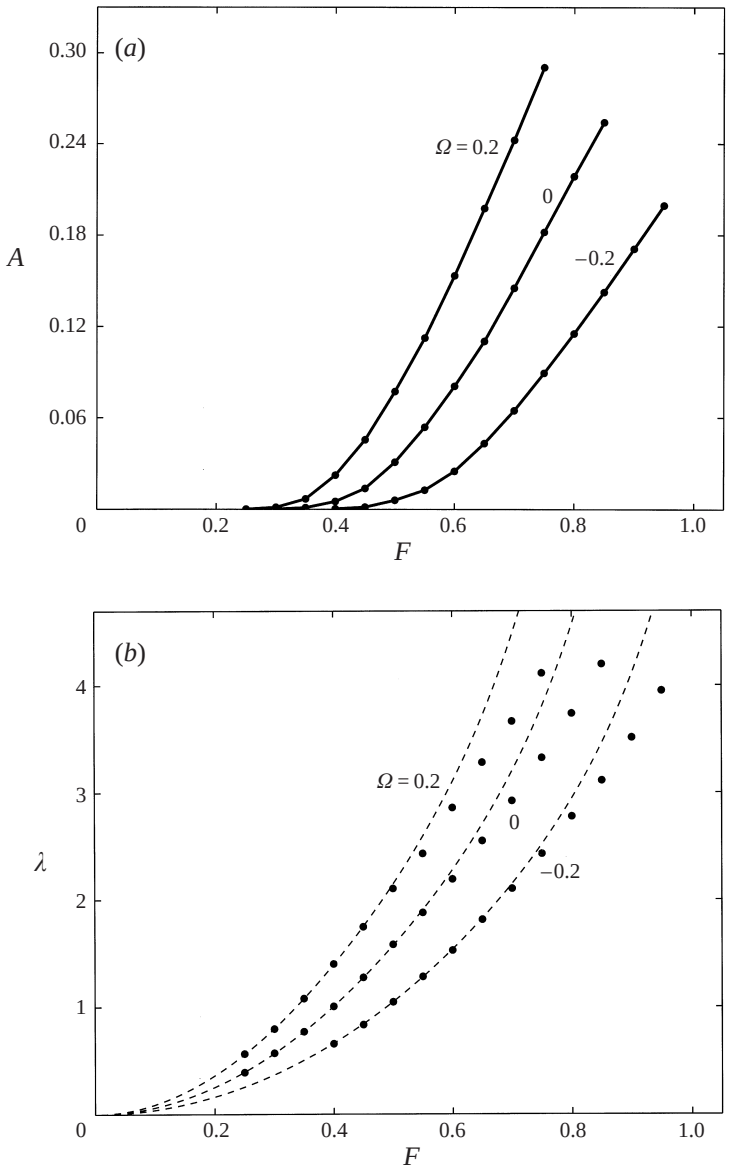

FIGURE 11. The dependence of the wave amplitude A (in a) and the wavelength λ (in b) on the Froude number F for three different values of the vorticity $\Omega = -0.2$, $\Omega = 0$ and $\Omega = 0.2$. Here $\gamma = 0.4$ and $\alpha = 0.1$.

evident, and it can be seen that the computed wavelength increases more slowly than that predicted by the linear theory.

Three plots of the wave amplitude versus the gap height for the Froude number fixed at $F = 0.5$ are presented in figure 12(a). Again, the plots from bottom to top correspond to vorticity values of $\Omega = -0.2$, 0 and 0.2 respectively. Here the Froude number is sufficiently small so that a gap height of $\gamma = 1$ is achievable for each value of the vorticity. As γ decreases, the amplitude of the waves decreases and then approaches some finite value as $\gamma \to 0$. The dependence of the wavelength on the

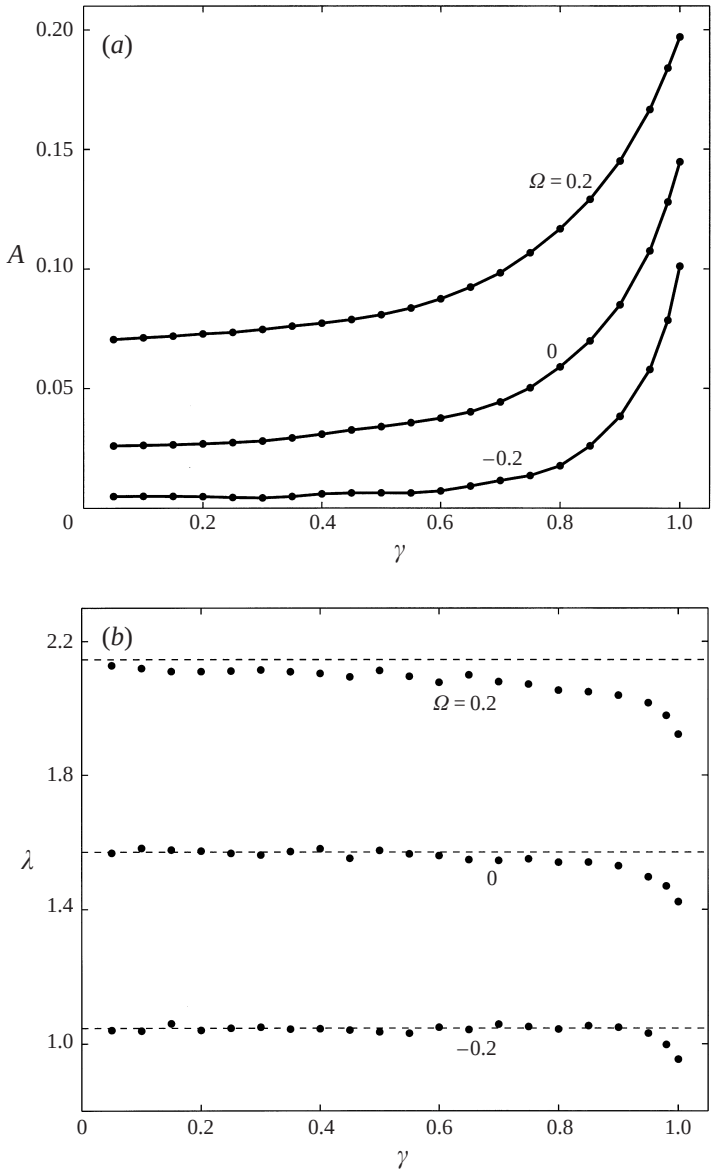

FIGURE 12. The dependence of the wave amplitude A (in a) and the wavelength λ (in b) on the gap height γ for three different values of the vorticity $\Omega = -0.2$, $\Omega = 0$ and $\Omega = 0.2$. Here $F = 0.5$ and $\alpha = 0.1$.

gap height for the same parameters is presented in figure 12(b). For fixed Froude number and vorticity, the predicted linear wavelengths are simply constants which are indicated by the dashed lines. The solid circles indicate that the computed wavelengths agree with the linear results for most values of the gap height γ, but decrease sharply as $\gamma \to 1$. Between $N = 601$ and $N = 741$ grid points were used when computing data for figure 12.

In the limit that the vorticity approaches the value $\Omega = -1$ from above, the velocities u and v on the free surface vanish and the free surface itself becomes flat at $y = 1$. No solutions were found for $\Omega \leqslant -1$. For fixed F and γ, the amplitude of

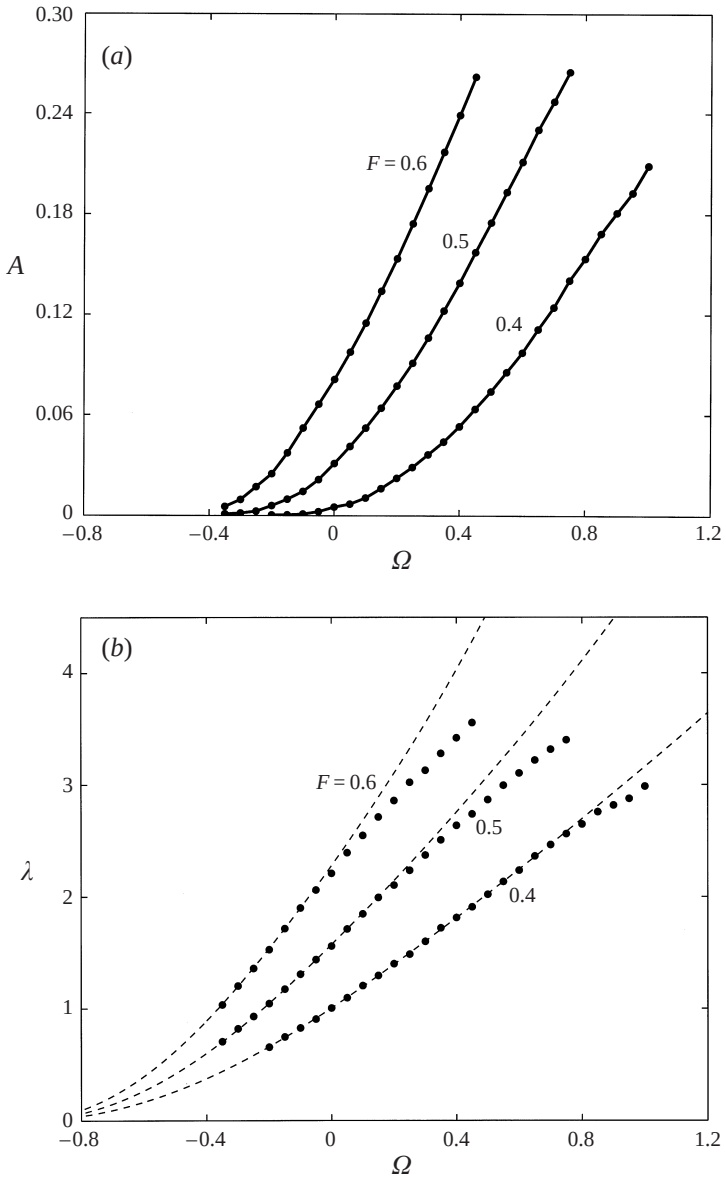

FIGURE 13. The dependence of the wave amplitude A (in a) and the wavelength λ (in b) on the vorticity Ω for three different values of the Froude number $F = 0.4$, $F = 0.5$ and $F = 0.6$. Here $\gamma = 0.4$ and $\alpha = 0.1$.

the waves increases from zero as the vorticity increases from -1. Again we expect there to exist some vorticity value at which the limiting configuration of breaking waves is reached. Figure 13(a) shows three typical relationships between the wave amplitude and the vorticity when the height of the body above the bottom is fixed at $\gamma = 0.4$. The plots from bottom to top correspond to Froude numbers $F = 0.4$, 0.5 and 0.6 respectively. For this figure, the number of mesh points used varied between $N = 601$ and $N = 1201$. The corresponding relationship between the wavelength and the vorticity is given in figure 13(b). Again, as before, the solid circles represent

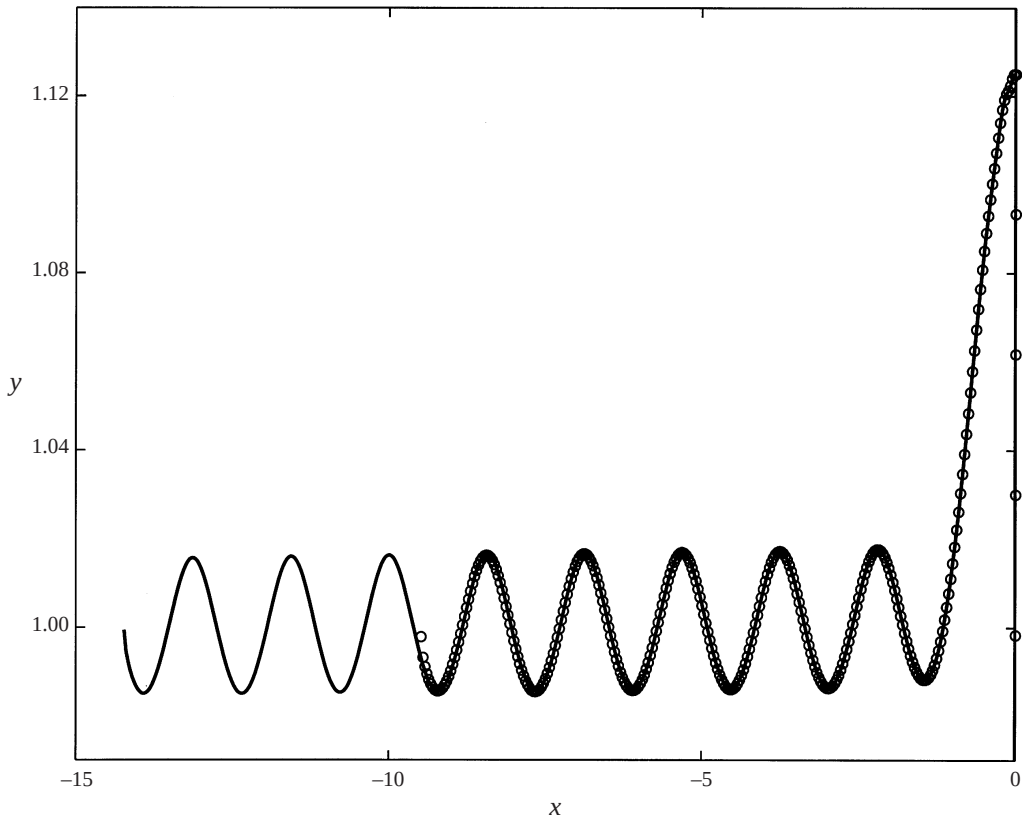

FIGURE 14. Free surface profiles for $F = 0.5$, $\Omega = 0$, $\gamma = 0.4$ and $\alpha = 0.1$. The grid size is the same for both cases, but the truncation point is different. One solution has been computed with $N = 601$ grid points, which are indicated by the circles. The other solution, which is computed with $N = 901$ grid points, is shown by the solid line.

the computed data while the dashed lines represent the linear wavelength. For small vorticity values, the linear prediction is valid, but as the vorticity increases, both sets of data begin to disagree, with the computed nonlinear wavelength increasing more slowly than the linear wavelength.

A few comments should be made here. First, periodic waves in a finite-depth fluid with constant vorticity have been calculated by Teles da Silva & Peregrine (1988). In their paper, exotic waves with overhanging profiles were presented for large vorticity values. These waves have limiting configurations where the wave profile has a point of contact with itself. No solutions have been found in the current problem which have waves that exhibit this sort of behaviour.

Secondly, no attempt has been made here to reproduce figure 10 for non-zero vorticity values, since it is expected that no new information would be gained from such a figure, and hence such an undertaking would not justify the large amount of computational time required. Also, there has been no documentation in the literature of data to fit an envelope curve similar to the one shown in figure 10 when the vorticity parameter Ω is non-zero. We therefore could not use such a figure to make any predictions about when the waves reach any sort of limiting configuration.

Finally, an example of the accuracy check used is shown in figure 14. Here two solutions are calculated with the same parameters and grid size but with a different

number of grid points and hence different truncation points upstream. The solid line indicates a solution computed with $N = 901$ points, while the circles indicate the location of the grid points for a solution with $N = 601$. We see that, with the exception of the first few mesh points upstream, both profiles are in good agreement with each other, which indicates that the result with $N = 601$ provides a sufficiently well converged solution.

4. Conclusions

In this paper, a boundary integral method has been used to calculate free surface flows past a bow-shaped body where the fluid is assumed to have a constant vorticity throughout. Supercritical bow flows have been found numerically and it is shown for most values of the vorticity that the behaviour of these solutions is qualitatively the same as those for the irrotational flow past a semi-infinite rectangle (see Vanden-Broeck 1989). That is, solutions can be found for values of γ (the height of the body above the bottom) up to some limiting value, at which stage the free surface attaches to the lowest point on the front face of the bow. In our configuration, the attachment height here is $y_a = \gamma + \alpha$, where α is the radius of the rounded corner. For sufficiently large vorticity values, however, there is no limiting solution, and the solution branches appear to terminate at some γ value for no obvious physical reason. The particular vorticity value corresponding to this change of behaviour was computed to be $\Omega = 0.33$ for the case when the corner radius is $\alpha = 0.2$.

On the other hand, no waveless bow flows could be found at all for subcritical Froude numbers. Nevertheless, when the radiation condition was dropped in the numerical method, solutions characterized by a train of waves upstream were found for fixed Froude number, body height and vorticity. A very detailed study of the properties of these waves has been presented here, and involved the computation of over 500 separate converged solutions, most of which used at least 600 grid points on the free surface and body, and some needed over 1000 grid points. The amplitude of the upstream waves was found to increase with both the Froude number and the vorticity and it is expected that these waves ultimately reach the Stokes limiting configuration with a 120° angle at their crests. A similar behaviour was encountered when the height of the body above the bottom γ was increased; however for all the values of Froude number and vorticity within our range of numerical capability, a solution with $\gamma = 1$ was found before the limiting configuration could be reached. No subcritical solutions for $\gamma > 1$ could be found.

It should be pointed out that since these subcritical flows violate the radiation condition, they cannot be classified as bow flows and hence must describe some sort of stern flow. In this respect, these solutions are analogous to those found for the flow under a sluice gate. Vanden-Broeck (1997) showed numerically, when the free surface meets a sluice gate at a stagnation point, that no waveless subcritical solutions exist. Instead, all the solutions computed were found to exhibit a train of waves on the upstream free surface. The only valid interpretation of these solutions must be that they correspond to the situation where the flow is reversed and the radiation condition holds, as is the case for the problem considered in this paper.

Our results show that there is at most one waveless solution for a situation where the vorticity and body draught are fixed, and the Froude number is allowed to be determined as part of the solution. It is then natural to ask what becomes of those waveless solutions when the Froude number is changed slightly. As stated in the introduction, it has been conjectured that in this situation a splash might appear at

the front of the bow. Another possibility is that a rolling 'forward wake' of constant vorticity may form on top of the free surface, as suggested by Tuck & Vanden-Broeck (1985). This configuration is currently being considered by the authors and the results will be presented at a later time.

The work of the first author has been supported by a University of Queensland Postgraduate Research Scholarship. The authors are indebted to anonymous referees for critical comments on this paper, resulting in the elimination of several errors. Thanks also to Adrian Koerber for his comments on the manuscript and useful discussions on nonlinear water waves.

REFERENCES

Asavanant, J. & Vanden-Broeck, J.-M. 1996 Nonlinear free-surface flows emerging from vessels and flows under a sluice gate. *J. Austral. Math. Soc.* B **38**, 63–86.

Benjamin, T. B. 1968 Gravity currents and related phenomena. *J. Fluid Mech.* **31**, 201–248.

Cokelet, E. D. 1977 Steep gravity waves in water of arbitrary uniform depth. *Phil. Trans. R. Soc. Lond.* A **286**, 183–230.

Dagan, G. & Tulin, M. P. 1972 Two-dimensional free-surface gravity flow past blunt bodies. *J. Fluid Mech.* **51**, 529–543.

Dias, F. & Vanden-Broeck, J.-M. 1993 Nonlinear bow flows with spray. *J. Fluid Mech.* **225**, 91–102.

Farrow, D. E. & Tuck, E. O. 1995 Further studies of stern wavemaking. *J. Austral. Math. Soc.* B **36**, 424–437.

Forbes, L. K. 1985 On the effects of non-linearity in free-surface flow about a submerged point vortex. *J. Engng Maths* **19**, 139–155.

Forbes, L. K. & Belward, S. R. 1996 Atmospheric solitary waves: some applications to the morning glory of the Gulf of Carpenteria. *J. Fluid Mech.* **321**, 137–155.

Forbes, L. K. & Hocking, G. C. 1993 Flow induced by a line sink in a quiescent fluid with surface-tension effects. *J. Austral. Math. Soc.* B **34**, 377–391.

Hocking, G. C. 1993 Bow flows with smooth separation in water of finite depth. *J. Austral. Math. Soc.* B **35**, 114–126.

Hocking, G. C. & Forbes, L. K. 1991 A note on the flow induced by a line sink beneath a free surface. *J. Austral. Math. Soc.* B **32**, 251–260.

Madurasinghe, M. A. 1988 Splashless ship bows with stagnant attachment. *J. Ship Res.* **32**, 194–202.

Madurasinghe, M. A. & Tuck, E. O. 1986 Ship bows with continuous and splashless flow attachment. *J. Austral. Math. Soc.* B **27**, 442–452.

McCue, S. W. & Forbes, L. K. 1999 Free surface flows emerging from beneath a semi-infinite plate in a fluid with constant vorticity. *J. Fluid Mech.* (submitted).

Mekias, H. & Vanden-Broeck, J.-M. 1989 Supercritical free-surface flow with a stagnation point due to a submerged source. *Phys. Fluids* A **1**, 1694–1697.

Mekias, H. & Vanden-Broeck, J.-M. 1991 Subcritical flow with a stagnation point due to a source beneath a free surface. *Phys. Fluids* A **3**, 2652–2658.

Schwartz, L. W. & Fenton, J. D. 1982 Strongly nonlinear waves. *Ann. Rev. Fluid Mech.* **14**, 39–60.

Teles da Silva, A. F. & Peregrine, D. H. 1988 Steep, steady surface waves on water of finite depth with constant vorticity. *J. Fluid Mech.* **195**, 281–302.

Tuck, E. O., Simakov, S. T. & Wiryanto, L. H. 1997 Steady splashing flows. *Abstract for 12th Intl Workshop on Water Waves and Floating Bodies, Marseilles, France, 1997.*

Tuck, E. O. & Vanden-Broeck, J.-M. 1985 Splashless bow flows in two dimensions? In *Proc. 15th Symp. Naval Hydrodynamics, Hamburg, 1984,* pp. 293–300. National Academy Press, Washington, DC.

Vanden-Broeck, J.-M. 1980 Nonlinear stern waves. *J. Fluid Mech.* **96**, 603–611.

Vanden-Broeck, J.-M. 1989 Bow flows in water of finite depth. *Phys. Fluids* A **1**, 1328–1330.

Vanden-Broeck, J.-M. 1994 Steep solitary waves in water of finite depth with constant vorticity. *J. Fluid Mech.* **274**, 339–348.

VANDEN-BROECK, J.-M. 1997 Numerical calculations of the free-surface flow under a sluice gate. *J. Fluid Mech.* **330**, 339–347.

VANDEN-BROECK, J.-M. & KELLER, J. B. 1987 Weir flows. *J. Fluid Mech.* **176**, 283–293.

VANDEN-BROECK, J.-M. & SCHWARTZ, L. W. 1979 Numerical computation of steep gravity waves in shallow water. *Phys. Fluids* **22**, 1868–1871.

VANDEN-BROECK, J.-M., SCHWARTZ, L. W. & TUCK, E. O. 1978 Divergent low-Froude-number series expansion in nonlinear free-surface flow problems. *Proc. R. Soc. Lond.* A **361**, 207–224.

VANDEN-BROECK, J.-M. & TUCK, E. O. 1977 Computation of near-bow or stern flows, using series expansion in the Froude number. In *Proc. 2nd Intl Conf. Numerical Ship Hydrodynamics, Berkeley, CA*, pp. 371–381. University Extension Publications.